Research Square

Preprints are preliminary reports that have not undergone peer review. They should not be considered conclusive, used to inform clinical practice, or referenced by the media as validated information.

Variability of Luminous QSOs following thermal timescale in standard thin accretion disk models

Ji-Jia Tang (ji-jia.tang@anu.edu.au)
Australian National University https://orcid.org/0000-0002-1860-0886

Christian Wolf
Research School of Astronomy and Astrophysics, The Australian National University, Canberra
https://orcid.org/0000-0002-4569-016X

John Tonry
University of Hawaii https://orcid.org/0000-0003-2858-9657

Article

Keywords:

Posted Date: May 3rd, 2022

DOI: https://doi.org/10.21203/rs.3.rs-1557549/v1

License: This work is licensed under a Creative Commons Attribution 4.0 International License.
Read Full License

Variability of Luminous QSOs following thermal timescale in standard thin accretion disk models

Ji-Jia Tang[1], Christian Wolf[1,2], and John Tonry[3]

[1]Research School of Astronomy and Astrophysics, Australian National University, Cotter Road Weston Creek, ACT 2611, Australia
[2]Centre for Gravitational Astrophysics, Australian National University, Building 38 Science Road, Acton, ACT 2601, Australia
[3]Institute for Astronomy, University of Hawaii, 2680 Woodlawn Drive, Honolulu, HI 96822-1897, U.S.A.

draft April 14, 2022

Abstract

We study the dependence of the stochastic variability of QSOs on luminosity, wavelength and thermal timescale in their accretion disks. We use over 5,000 of the most luminous known QSOs with light curves of almost nightly cadence spanning > 5 years of observations from the NASA/ATLAS project, which provides 2 billion magnitude pairs for a bootstrap analysis. The results depend on which timescales are included in the analysis: when we only consider timescales > 6 months, we find a robust behaviour for the whole sample. This behaviour is consistent with an un-damped random walk on the thermal timescales predicted by thin-disk models. We find a variability amplitude of $\log(A/A_0) \approx 1/2 \times \log(\Delta t/t_{\rm th})$. On shorter timescales, we observe a suppression of the amplitude due to light travel-time filtering, which could be used to measure sizes of accretion disks.

Every galaxy in the Universe contains a supermassive black hole (SMBH) at its centre; their origin and growth is one of the biggest mysteries in astronomy. Most black holes appear dark and are revealed only by their gravity[1]. During growth spurts, however, matter from surrounding areas falls towards the black hole. Its gravitational energy is turned via heat into radiation, which highlights the black hole as a "QSO" (Quasi-Stellar Object). Fast-growing black holes are the most luminous objects in the Universe. At UV-optical wavelengths, QSOs can outshine 1,000 large galaxies[2,3].

The key for turning gravitational energy into heat is matter flowing through an accretion disk[4]. Matter orbiting the black hole drifts inwards as high friction in the disk dissipates orbital energy. It is now clear that Keplerian disks with weak magnetic fields are prone to magneto-rotational instability (MRI)[5]. MRI is a fundamental instability converting differential rotation into turbulent fluid motions, feeding an energy cascade, and explaining the anomalously high viscosity needed for QSO disks[6].

Accretion disks are an elegant explanation for the high luminosity and compactness of QSOs. A standard model of optically thick and geometrically thin disks predicts their temperature profiles and emission[7]. But they are too small to be observed with any spatial resolution by current facilities. Therefore, we seek clues about their properties from the variability of their UV-optical brightness. The variability is ubiquitous on all timescales, although viscous timescales in QSO disks are longer than human lifetimes[8]. While this has been a puzzle, MRI must be a source of short-term fluctuations. Separately, rapid variability has also been linked to highly fluctuating heating from the X-ray corona near the event horizon of the black hole[9–11].

Monitoring of QSO samples has revealed that fluctuations can be described by a 'damped random walk' model[12–14]: brightness changes tend to be larger when the time delay between any two measurements is longer. However, this model provides only a behavioural analogy and no physical insight. Mathematically, the light curve (LC) of an object, or a sample, can be statistically described by a variability "structure function" (SF): the typical brightness difference is expressed as a function of time interval[15,16]. The SFs of QSOs are characteristically different from other types of variable objects, so that QSOs can be identified in a time-domain survey by the SF alone[17].

Measurements of the SF agree on two trends: fluctuations on a fixed timescale get stronger in less luminous QSOs, and for a given QSO, they get stronger when bluer parts of the emission are monitored[13,18–21]. This is described by an SF of the form

$$\log A = B_0 + \gamma \times \log \Delta t + B_L \times \log L + B_\lambda \times \log \lambda \,, \tag{1}$$

where amplitudes A of flux changes are in terms of magnitude, and L is the measured luminosity of the QSO. Both the time separation between the two measurements, Δt, and the wavelength of observed light, λ, are expressed in the QSO rest-frame, i.e., with cosmological redshift and time dilation removed.

While past works agree that $B_L < 0$ and $B_\lambda < 0$, they disagree on the strength of the trends. Some complicating factor may not be controlled for in existing studies. The parameter $\gamma = d\log A/d\log \Delta t$ at fixed (L, λ) describes the damping in the random walk and is reported in the range of 0.2 to 0.5. Then, $B_L = d\log A/d\log L$ at fixed $(\Delta t, \lambda)$ describes the dependence on disk luminosity (and hence size); it is reported in the range of -0.33 to -0.16. Finally, the parameter $B_\lambda = d\log A/d\log \lambda$ at fixed $(\Delta t, L)$ describes the trend with wavelength and thus location of the fluctuating source within the disk; it is measured in the range from -0.75 to -0.44, although observations of non-linear relations also include slope values outside this interval.

Here, we present a new analysis of the variability structure function of the $\sim 5,000$ brightest QSOs in the sky using light curves with unprecedented sampling. The data are from the 0.5-metre NASA/ATLAS telescope (Asteroid Terrestrial-impact Last Alert System[22]), which was built to find dangerous asteroids that might threaten the Earth. ATLAS is designed to image the entire sky seen from its location in Hawaii four times every night, weather permitting. With up to 1,200 nights per QSO per band, we get ~ 2.1 billion magnitude pairs to constrain the QSO SF. This must be one of the best data sets for studying QSO variability before the Vera C. Rubin Telescope operates.

Results

The new light curves include observations from 2015 to 2021 in two passbands, cyan and orange (centred on 533 and 679 nm, respectively). We limit the sample to redshift $0.5 < z < 3.5$ ($z < 2.4$ in the cyan band), where QSOs are luminous enough so that their host galaxies will not affect the measurements. We reject radio-loud QSOs, where variability may be enhanced by shocks in jets and mask the pure accretion disk behaviour[23]. We also reject gravitationally lensed QSOs, for which we would observe blended light curves. We finally reject QSOs with close neighbours as seen by the ESA Gaia astrometry mission[24], as their light curves could be disturbed by neighbours.

Previous works typically fitted a global model for the SF, such as equation 1, to the whole data set. The richness of this new data set, however, offers the alternative to split the data into subsets without incurring the penalty of noisy statistics. At $\Delta t = 100$ days, we can compare our SF with one source in the literature[20] and we find very good agreement as a function of wavelength and also luminosity, where our overlap is ~ 1 dex. Crucially, we split our data into twenty bins in Δt and fit the trends with luminosity and wavelength separately for each bin, using the equation

$$\log(A(\Delta t)) = B_{0,\Delta t} + B_{L,\Delta t} \times \log L + B_{\lambda,\Delta t} \times \log \lambda \,. \tag{2}$$

Thus, we get twenty different estimates for B_L and B_λ, independently for each Δt bin. As we can now study the trends on different timescales, we may see different regimes of behaviour. At the short Δt end, we use the variability measured on timescales of 1 day to estimate the noise in the observations. At the long end, window effects from the finite length of the observed light curves may cause noise in the parameters. Since we observe here the most luminous QSOs, which harbour the most massive accreting black holes known in the Universe, we do not yet see much of the damping timescale, which has been found to depend on black hole mass[25]. We restrict the wavelength range to longer than 130 nm (avoiding flux from the strong Ly-α emission line) and shorter than 300 nm (avoiding a previously seen upturn in variability[13,18,20]). We use two types of statistical analysis, one forming simple bin averages, and another using a computationally more intense bootstrap analysis.

Figure 1 shows the resulting parameters for a range in Δt from 10 to 337 days. Both methods of analysis produce consistent estimates. The estimates for B_L and B_λ show a strong trend with Δt. It is immediately clear that a global fit will produce estimates for B_L and B_λ that depend on the fitting range in Δt and on the distribution of pairs in the range, and thus on subtleties of survey cadence. We suggest this fact explains the variety of estimates obtained in past works, while their actual data were likely consistent. We obtain fiducial global estimates for B_L and B_λ by choosing different fitting ranges for Δt. Figure 2 shows the effect of wider windows and demonstrates how results depend on the range of behaviour forced into a single global fit.

In this work, having controlled for Δt by fitting the trends in each bin separately, we reveal *two* regimes in behaviour: a shorter-Δt regime, where both B_L and B_λ drift with Δt, and a longer-Δt regime, where they both remain constant. Thus, the exact choice of fitting range in Δt will affect the parameter estimates very little in the longer-Δt regime. Here, we find fit parameters that appear close to $\gamma \approx 1/2$, $B_L \approx -1/4$ and $B_\lambda \approx -1$.

Structure functions on thermal timescales

So far, B_L and B_λ have described how variability amplitudes behave at fixed Δt. We can also look at the timescales, on which disks of different L, observed at different λ, show a fixed amplitude A. We find these timescales to behave similar to:

$$C_L = -d\log\Delta t(A)/d\log L = -B_L/\gamma = 0.539 \pm 0.004 \quad (3)$$

$$C_\lambda = -d\log\Delta t(A)/d\log\lambda = -B_\lambda/\gamma = 2.418 \pm 0.022\,. \quad (4)$$

The predicted temperature profile in thin disks[7], $T(r) \propto r^{-4/3}$, sets a mean radius for the origin of radiation and thus a mean thermal timescale $t_{\rm th}$ of the emitting surface, given λ and a size, and thus L, of the disk:

$$\log t_{\rm th} = c + 1/2\log L + 2\log\lambda\,. \quad (5)$$

The resemblance of our finding suggests that we rephrase equation 1 and express the SF with time intervals in units of the thermal timescale:

$$\log(A/A_0) = \gamma_{\rm th}\log(\Delta t/t_{\rm th})\,. \quad (6)$$

We determine $t_{\rm th}$ for each QSO and band given its (L, λ). Figure 3 shows the resulting SF expressed both in natural time and with a $t_{\rm th}$-scaled clock. Here, we increased the time resolution but reduced noise by grouping QSOs into subsamples of split by (L, λ). The wide (L, λ)-range of our sample causes a wide range of amplitudes at fixed Δt, but at fixed $\Delta t/t_{\rm th}$ we find indeed a tight range. At short timescales, the distribution appears suppressed relative to an SF with a fixed slope $\gamma_{\rm th}$, which will be discussed further below.

Seeing the short-term suppression of the variability amplitude and how it depends on the properties of the disk, we define the list of input data for our final global fit of the structure function. We use all combinations of QSOs and Δt bins, where the points in Fig. 3 are at $\log A > -1.4$; this seems to select the linear portion of the structure function. We find a bootstrap slope with natural clock time of $\gamma = 0.503 \pm 0.001$ and with a clock in units of a thermal timescale of $\gamma_{\rm th} = 0.510 \pm 0.002$, extremely consistent with the $\gamma = 1/2$ of an *un*-damped random walk.

QSOs as standard flicker candles

Crucially, the transition from a regular clock to a thermal time-scaled clock standardises QSOs: now the wide dispersion seen among QSOs with a variety of luminosities and observing passbands disappears and QSOs follow a single characteristic behaviour with thermally scaled time. The SF of QSOs are then an intrinsically tight relation when expressed in units of thermal timescale. In observation, this template SF relation will be broadened principally by two factors that bias the estimated luminosity of individual QSOs and thus their thermal timescales: (1) the disks in our sample are viewed under a range of inclination angles i, from a pole-on view, with $i = 90°$ and maximum projected disk surface, to highly inclined views, perhaps with $i \approx 20°$. The observed luminosity of an optically thick 2D surface emitting blackbody radiation is

proportional to its projected area, hence $L_{\rm obs} = L_{\rm true} \sin i$. In detail, a flaring disk with greater thickness in the outer parts and limb darkening effects modify this relation. We expect the range in inclination to cause at least a factor of 3 range in luminosity bias and thus a $\sqrt{3}\times$ range in a thermal timescale bias. (2) In addition, the disks are seen through a range of dust extinction levels from the QSO host galaxies. Even a moderate reddening range of $E(B-V) = 0.0 \ldots 0.1$ translates into a factor 2 range of UV luminosity and adds another $\sqrt{2}$ range in thermal timescale bias.

A measured pair of SF and luminosity could be used as an orientation indicator for an accretion disks. A template SF would be described by a single value of A_0. The deviation of a measured SF for an individual QSO could then be absorbed into a scale factor for the clock, $f_t = (\Delta t_{\rm needed}/\Delta t_{\rm data})$, that is needed to match the template. The factor f_t could then constrain the disk inclination. Uncertainties in estimating the dust extinction, perhaps from accretion disk SEDs[26,27], may set the floor to the precision of inclination estimates that can be achieved with this method.

Light-travel time filtering

As shown in Figure 3, at shorter Δt our SFs have lower amplitudes than extrapolated with a constant slope $\gamma_{\rm th}$, and we also saw the trend parameters B_L and B_λ drifting with Δt at shorter timescales. In this regime, we expect observations of intrinsic variability to be filtered by light-travel time effects. With any accretion disk that is not seen pole-on, every disk annulus of fixed distance from the black hole will cover a range of distances to the observer. Hence, the observer will see the accretion disk not as it appears in one instance, but a time-filtered version of the intrinsic light curve, according to the range of iso-delay surfaces.

If there is any synchronicity of variability within an annulus as caused, e.g., by the lamppost model, the SFs will show an intrinsic random-walk regime only at longer Δt, but a light-travel time filtered amplitude suppression at shorter Δt, and a knee in the SF that correlates with the travel time difference $\Delta t_{\rm light} \approx (r_{\rm disk} \sin i)/c$ resulting from the size and inclination of the disk. Variability amplitudes are suppressed more when we look at larger annuli, as we do for disks with larger L and passbands probing larger λ. In Figure 3, the largest disks (those with the longest $t_{\rm th}$ are shown in red) having their random-walk behaviour suppressed up to the longest $\Delta t_{\rm knee}$ values. As a result, the values of B_L and B_λ appear more negative in Fig. 1 than they are intrinsically.

We propose that this short-term suppression of apparent variability amplitudes and the location of the knee in the SF can be used to constrain the sizes of accretion disks. A detailed analysis of this aspect is deferred to a separate study. This new method is independent of the known method of disk reverberation mapping. The latter is an attempt to constrain disk sizes with multi-band light curves that monitor the disk from its inner hotter regions to its outer cool regions. It exploits the fact, that the X-ray corona around the event horizon of a black hole is the region with the highest temperatures and energy densities. It is also on the smallest observable scales and known to be highly variable. As the hot X-ray corona pumps rapidly variable amounts of extra heat into the disk, the disk responds with a simple light-travel time delay. This mechanism has explained observations of some Seyfert galaxies[10,11], but results on QSOs do not yet agree[28–31]. It will be interesting to compare results from the two methods in the future.

Outside our wavelength interval

When we study the wavelength dependence at $\lambda > 300$ nm, we notice an upturn in A, relative to a trend of $B_\lambda \approx -1$, which has been seen before[13,18,20,32], see also Figure 4, right panel. Fluctuations in the outer, cooler parts of QSO accretion disks appear to be enhanced by an additional mechanism. This may be related to the ionisation state of the cooler gas, or it could indicate a change in the temperature profile. The heating from the X-ray corona is expected to reduce the temperature decline in the outer, cooler parts of flaring disks, and thus change the thermal timescales.

Also, we have excluded $\lambda < 130$ nm, as we cannot disentangle light from the disk continuum and light from the broad Ly α line. This translates into excluding pivot wavelengths in the passbands of $\lambda < 160$ nm. The inner disks emitting such light will be harder to study as a wider wavelength range in the UV domain is absorbed by intervening gas along the line-of-sight to QSOs.

Conclusion

Our principal result is that the observed variability of QSO continuum emission in the restframe UV appears consistent with an *un*-damped random-walk behaviour on thermal timescales of the emitting material. The mean amplitudes of fluctuations can be described by $\log(A/A_0) = 1/2 \times \log(\Delta t/t_{\rm th})$. This appears consistent with an origin of the fluctuations in magneto-rotational instabilities (MRI) in differentially rotating accretion disks that are made of magnetised plasma; there, the equations of motion scale only with the orbital timescale, which is proportional to the thermal timescale[6,33].

The results appear consistent with the temperature profiles of thin-disk models[7], at least at wavelengths from 130 to 300 nm. Deviations are seen at longer wavelengths that represent the cooler, outer parts of disks. MRI is suggested to produce variability with a random walk phenomenology, and early simulations have suggested $\gamma \approx 0.4 \ldots 0.5$[34]. Disks could thus be ordered in a 1-parameter family with the mean thermal timescale at a chosen wavelength as an ordering parameter. The SF of QSOs may then be a universal and intrinsically tight relation, broadened in observation by disk orientation and dust extinction affecting the inferred luminosity.

We also observe a knee in the SF, where at shorter timescales the observed variability appears suppressed by light-travel time filtering. We propose that observations of this knee are a new method to reveal the sizes of accretion disks when their inclination is taken into account.

Currently, it is unclear to what relative extend the variability of QSO accretion disks is composed of the internal MRI instability vs. disk reprocessing from the externally driving hot X-ray corona. This relative share might also depend on disk luminosity. It has been argued that more X-ray powerful objects seem to relate to an increased UV variability only on timescales much longer than the expected light travel time[35], which may be disfavour the reprocessing model in luminous QSOs.

In the near future, observations of QSOs with the forthcoming powerful 10-year Legacy Survey in Space and Time (LSST[36–38]) are awaited to provide more insights. LSST u band data could also probe light shortwards of Ly α at suitable redshifts. The

much reduced photometric errors in LSST will allow to determine how tight and universal the UV variability structure function really is. QSO accretion disks could be standard flicker candles, whose variability reveals their true luminosity and becomes a disk orientation indicator. This would be a massive step towards more accurate measurements of the physical properties of QSOs, their emission-line regions and their accretion disks. This includes luminosity, accretion rate and radiative efficiency, as well as measuring the masses of their black holes better.

Online Methods

QSO sample and data cleaning

We combine the Million Quasars Catalog[39] (MILLIQUAS v7.1 update) with the *Gaia* eDR3 catalogue[24] and select 6,163 spectroscopically confirmed, non-lensed QSOs with Gaia magnitude $Rp < 17.5$, redshift $0.5 < z < 3.5$, declination $\delta > -45°$, Galactic foreground reddening[40] of $E(B-V)_{\rm SFD} < 0.15$ and Gaia BpRp Excess Factor < 1.3 (indicative of single, unblended, point sources); we also require that the MILLIQUAS and Gaia positions are coincident within $0.3''$, which excludes blended objects of similar SED such as the multiple images of lensed QSOs, and that sources have no Gaia neighbours within $15''$ to keep the ATLAS photometry unaffected. The ATLAS photometric system from counts to Jy is consistent with all extant sources of photometry including Pan-STARRS and Gaia[41]. After matching with the source list from NASA/ATLAS, 6,115 QSOs remain.

The selection and luminosity estimates are based on Gaia eDR3 mean photometry, which is arguably the best-calibrated among all large astronomical datasets[42]; it is based on Gaia observations from mid-2014 to mid-2017, which overlaps with the period of the ATLAS lightcurves. Thus, there will be no noticeable selection bias in favour of QSOs that might be brighter during an early selection epoch but fainter during a much later light curve observation[43]. From ATLAS, we use point-source photometry for all available epochs, which is appropriate for isolated point-source objects such as the most luminous QSOs.

We further clean our QSO sample with the following criteria: six QSOs removed due to large flux errors (90-percentile flux errors in the ATLAS orange band LC of $\sigma_{f_\nu,\rm o} > 150\mu$Jy or in the ATLAS cyan band LC of $\sigma_{f_\nu,\rm c} > 85\mu$Jy). On individual images, ATLAS reaches a signal-to-noise ratio (SNR) ~ 11 in the orange passband and ~ 13 in the cyan passband for the faintest objects in the sample. Up to four such images are available per night.

In order to reject radio-loud QSOs, we cross-match the sample with the radio catalogues from Faint Images of the Radio Sky at Twenty-cm[44] (FIRST), NRAO VLA Sky Survey[45] (NVSS), and Sydney University Molonglo Sky Survey[46] (SUMSS). We use matching radii between MILLIQUAS and FIRST, NVSS, and SUMSS coordinates of 3", 12", and 11", respectively. 1,242 QSOs are matched with at least one of the radio catalogues. If a QSO is matched to multiple radio sources in NVSS or SUMSS, the radio detection with the closest separation is used. We apply a radio loudness criterion of $0.4 \times (m_o - t_{\rm NVSS/SUMSS}) > 1.3$ as radio loud for NVSS or SUMSS matched QSOs. Sources below the criterion are radio intermediate. All QSOs matched with FIRST only are radio intermediate. The sample contains 775 radio-loud and 467 radio-intermediate objects, and 4,848 radio non-detections. For a subsample of 910 objects, we inspect visually the spectra in the Sloan Digital Sky Survey[47] (SDSS) and the Large Sky Area Multi-object Fiber Spectroscopic Telescope (LAMOST) QSO survey[48] and confirm that the objects are QSOs indeed. The final sample for the analysis in this work consists of 5,315 QSOs.

We clean the ATLAS LCs with the following steps: first, we exclude observations with large errors of $\log(\sigma_{f_\nu,\rm o}) > -3.94 - 0.12 \times (m_{\rm o} - 16.5)$ and $\log(\sigma_{f_\nu,\rm c}) >$

$-4.17 - 0.10 \times (m_{\rm c} - 16.5)$, which constitute about 5 percent of all observations. Second, we compare each measurement with other observations within ± 7 days and remove outliers with a 2σ-clipping to reject spurious variability, e.g., due to temporary chance blending with faint asteroids. If there is only one observation within ± 7 days, it is kept for further analysis.

Luminosity

For calculating luminosities, we apply a correction for dust extinction[40] using bandpass coefficients[49] of $R_{Bp} = 3.378$ and $R_{Rp} = 2.035$. We adopt a flat ΛCDM cosmology with $\Omega_{\rm m} = 0.3$ and a Hubble-Lemaître constant of $H_0 = 70$ km sec^{-1} Mpc^{-1} to calculate luminosity distances. We measure the luminosity at a restframe wavelength of 3,000 Å using a linear interpolation of the Gaia Bp and Rp magnitudes. At redshifts of $0.5 < z < 0.7$ and $z > 1.56$, the restframe 3,000 Å point is extrapolated beyond the pivotal wavelengths of the Gaia filters, although the point is within the Gaia filters at all redshifts. Luminosity errors from this procedure are expected to be $< 20\%$ and thus much smaller than those introduced by host galaxy dust and the orientation of the disk (up to a combined factor 6). Bolometric luminosities, as used by some authors[20], are derived with $\log(L_{\rm bol}/L_{3000}) = \log(f_{\rm BC} \times \lambda) = \log(5.15 \times 3000\text{Å}) = 4.189$, using $f_{\rm BC} = 5.15$ as the bolometric correction factor[50].

Thermal timescale

For each QSO and passband, we estimate the mean thermal timescale of the section in its accretion disk that dominates the light contribution to the passband. By combining the equation for $t_{\rm th}$[33] and an equation for the scale length of the disk given L, λ values[51], we get:

$$\begin{aligned} \frac{t_{\rm th}}{\rm days} &= \frac{2.89}{1.8} \times \frac{1}{86400} \times 10^{-13} \times \left(\frac{45 G M_\odot f_{\rm BC} \lambda_{3000} L_{3000} \lambda_{\rm rf}^4}{16\pi^6 \alpha^2 \eta h_p c^4}\right)^{0.5} \\ &= 6.22 \times 10^{-28} \times \left(\frac{L_{3000}}{\rm erg/s/\text{Å}}\right)^{0.5} \times \left(\frac{\lambda_{\rm rf}}{\text{Å}}\right)^2 , \end{aligned} \tag{7}$$

where h_p is the Planck constant, $\alpha = 1$ is the assumed viscosity parameter in the thin-disk model. We assume a radiative efficiency of $\eta = L_{\rm bol}/(\dot{M}c^2) = 0.1$, where $\dot{M}$ is the mass accretion rate, and we argue that changes in η will not affect this analysis noticeably: changes in η would be due to variations in black-hole spin affecting the inner cutoff of the accretion disk. For a given $\dot{M}$, such a change would not change the appearance of the outer disk, and would change only little the overall emitted $\lambda_{3000} L_{3000}$ and the thermal timescale at the wavelengths observed here. Instead, it would affect the emission of higher-energy photons and mostly change the $L_{\rm bol}$ and thus the bolometric correction, so $f_{\rm BC}/\eta$ should be close to constant under variations of η. Any mismatch between the values for $f_{\rm BC}$ and η chosen here, will globally re-scale the $t_{\rm th}$ for all our QSOs with a fixed constant.

Variability structure function

We adopt the following definition of the variability structure function (SF)[52]:

$$A = \sqrt{\frac{\pi}{2} < \Delta m >^2 - < \sigma^2 >}, \text{ with } \Delta m = |m_{\rm i} - m_{\rm j}|, \tag{8}$$

where $m_{\rm i}$ and $m_{\rm j}$ are two independent observations and σ is the variance of the noise. We find that the formal ATLAS magnitude errors appear underestimated and derive the σ^2 from the apparent variability measured from the multiple measurements within a day, because we expect the intra-day variability of radio-quiet QSOs to be negligible. We find $< \sigma^2 >$ as a function of observed magnitude, $m_{\rm obs}$, so that the SF is anchored at $A \approx 0$ for $\Delta t < 1$ day. The required noise model is shown in Figure 5 and given by

$$\log(< \sigma^2 >) = n_0 + n_1 m_{\rm obs} \ , \tag{9}$$

with the (n_0, n_1) being $(-12.411, 0.585)$ and $(-12.428, 0.573)$ for the orange and cyan passband, respectively. With only Poisson noise, n_1 is expected to be 0.4.

After examining the pair sampling distribution of all LCs, we aim to reduce window effects by ignoring pairs with $\Delta t_{\rm obs} \geq 0.47 \max(\Delta t_{\rm obs})$ in each QSO LC. Note that this cut is applied in the observed frame while the rest of the paper uses the rest-frame $\Delta t = \Delta t_{\rm obs}/(1+z)$, corrected for cosmological time dilation.

Binning

We have two methods of binning the data for different purposes. The first method is used for exploring the relation between SF and Δt, see Equation 2 and Figures 1, 2 and 4. The second method is used for fits over the final fitting range and for exploring the structure function as $f(\Delta t/t_{\rm th})$, see Equation 6, Figure 3 and Table 1.

In the first method, we split the Δt axis into 20 bins. The first Δt bin contains all pairs with $\Delta t < 1$ day, which is used only for noise analysis. Further bins are chosen to balance the number of pairs among the bins. The average number of pairs per Δt bin are $\sim$103 million and $\sim$8 million for orange and cyan passbands, respectively. We split the z axis into 9 bins, thus grouping QSOs with observations of similar restframe wavelengths. In the cyan passband, we exclude QSOs at $2.4 < z < 3.5$ to avoid contamination from Ly α line variability. In the orange passband, this range is the highest-z bin, but with few QSOs at high redshift this bin has low significance. QSOs at $0.5 < z < 2.4$ are grouped into 8 further z bins with roughly balanced QSO numbers. In each z bin, QSOs are further split into ten L_{3000} bins, each with almost equal QSOs numbers. In total, there are 1,800 bins in $(z, L_{3000}, \Delta t)$. In each bin, the mean value of z and L_{3000} and the mid-point of Δt is used for the analysis and figures.

In the second method, we split the Δt axis into 100 bins. The shortest $\Delta t < 1$ bin is exactly the same as in the first binning method, and further bins are balancing the number of pairs among the bins for both passbands. The QSOs are grouped into 16 bins along the $t_{\rm th}$ axis with an equal number of QSOs per bin, which is 2,950 and 4,134 in orange and cyan, respectively. In the $\Delta t/t_{\rm th}$ axis, we split the observed pairs into 100 bins of constant number, independently for each $t_{\rm th}$ group in each passband

after excluding pairs with $\Delta t < 1$ and $\Delta t > 337$ days. Combining both passbands, there are in total 3200 bins for $(t_{\rm th}, \Delta t)$ and separately 3200 bins for $(t_{\rm th}, \Delta t/t_{\rm th})$. In each bin, the mid-point of Δt and $\Delta t/t_{\rm th}$ is used for the analysis and figures.

Simple bin averages method

For each individual QSO, we calculate its SF with equation 8 from all available pairs in each Δt or $\Delta t/t_{\rm th}$ bin. Note that the $< \Delta m >$ is the 3σ-clipped mean of magnitude differences. Then, for each $(z, L_{3000}, \Delta t)$ or $(t_{\rm th}, \Delta t)$ or $(t_{\rm th}, \Delta t/t_{\rm th})$ bin we calculate the median amplitude and the standard error of the median (SEMED) on the A^2 scale, which ensures that QSOs with negative noise-corrected amplitudes A^2, due to an over-subtraction by the $\langle \sigma^2 \rangle$ noise model, are still included in the statistics. These are used as the representative amplitude A and its error in the later population fitting.

Bootstrap method

Using bootstrapping, we can account better for the contribution of each QSO. Here, we select random pairs in each of the $(z, L_{3000}, \Delta t)$ or $(t_{\rm th}, \Delta t)$ or $(t_{\rm th}, \Delta t/t_{\rm th})$ bins. We randomly pick a QSO N times from all the QSOs in that bin, where N is the total number of QSOs in that bin. For each picked QSO, we randomly select 300 distinct pairs in the orange and 30 distinct pairs in the cyan passband, and then calculate the SF using equation 8. This process is repeated 100 times to get the bootstrap distribution, from which we calculate the mean and standard deviation for each bin.

SF fitting

In exploring the relation between SF and Δt, we preform a multi-variant fit with equation 10 to the (z, L_{3000}) bins in each Δt bin:

$$\log(A(\Delta t)) = B_{0,\Delta t} + B_{L,\Delta t} \log(\frac{L_{3000}}{10^{42.7}{\rm erg/s/\AA}}) + B_{\lambda,\Delta t} \log(\frac{\lambda_{\rm rf}}{2200\AA}) \ . \quad (10)$$

The $\log A$ and its 1-σ error is either from the bin averages or the bootstrap method. The $\lambda_{\rm rf}$ is from the pivotal wavelength of the passband divided by the $1 + z$. The normalisation factors for $\lambda_{\rm rf}$ and $\log(L_{3000})$ are chosen to be close to the median of the fitted sample. Data with $\lambda_{\rm rf} > 3000$Å behaves differently, and is excluded from the fit. We show an example of the result in Figure 4. In the left and middle panels of Figure 4, we group all L_{3000} bins for each redshift bin, and separate for orange and cyan passbands, and show the linear relation between $\log A$ and $\log(L_{3000}) - 42.7$ using the slope $B_{L,\Delta t}$. In the right panel of Figure 4, we present the intercepts of the linear relation for different $\log(\lambda_{\rm rf})$. We show the linear relation between those intercepts and $\log(\lambda_{\rm rf}/2200\AA)$ at $\lambda_{\rm rf} < 3000$Å. Note the upturn at longer wavelengths, which is compared here with results from the literature[20]. We compare the $B_{0,\Delta t}$, $B_{L,\Delta t}$, and $B_{\lambda,\Delta t}$ and their 1-σ errors from each Δt bin and show the result in Figure 1.

Table 1: Coefficients for final fit results.

method	bootstrap	bin averages
B_0	-0.925 ± 0.001	-0.965 ± 0.002
B_L	-0.271 ± 0.002	-0.277 ± 0.004
B_λ	-1.216 ± 0.011	-1.261 ± 0.022
γ	$+0.503 \pm 0.002$	$+0.447 \pm 0.003$
C_L	$+0.539 \pm 0.004$	$+0.620 \pm 0.010$
C_λ	$+2.418 \pm 0.022$	$+2.819 \pm 0.052$
A_0	-1.718 ± 0.002	-1.694 ± 0.003
$\gamma_{\rm th}$	$+0.510 \pm 0.002$	$+0.465 \pm 0.003$

Parameter averages in different, broad Δt windows

We fit equation 11 to $(z, L_{3000}, \Delta t)$ bins with $\lambda_{\rm rf} < 3000$Å:

$$\log(A) = B_0 + B_{\rm L} \log(\frac{L_{3000}}{10^{42.7}{\rm erg/s/Å}}) + B_\lambda \log(\frac{\lambda_{\rm rf}}{2200{\rm Å}}) + \gamma \log(\frac{\Delta {\rm t}}{216{\rm day}}) \quad (11)$$

We test the robustness of the parameter averages for B_L, B_λ, C_L and C_λ in the long regime by varying the lower edge, Δt_0, in defining the long regime, while leaving the upper Δt=337 days edge unchanged. The different results for B_0, B_L, B_λ, γ, C_L, and C_λ with their 1σ-errors for the bootstrap are shown in Figure 2.

The structure function as $f(\Delta t)$ and $f(\Delta t/t_{\rm th})$

For Figure 3 we use Δt bins as described above. The 32 QSO groups are ranked by $t_{\rm th}$ mixing both orange and cyan. We then fit Equation 1 using the same normalisation factors as in Equation 11 to the points with $\log A > -1.4$ using the 1-σ errors of $\log A$ for weighting (see Table 1 for results). We show this fit as a line in the left panel of Figure 3 by reusing the best-fit γ and refitting a mean $\log A$ offset to the same data without considering L and λ as parameters. In the right panel, we similarly fit the bins with $\log A > -1.4$ to equation 6 and show the fit as is (see Table 1 for results).

References

[1] Kormendy, J. & Ho, L. C. Coevolution (or not) of supermassive black holes and host galaxies. ARA&A **51**, 511–653 (2013).

[2] Richards, G. T. *et al.* The sloan digital sky survey quasar survey: Quasar luminosity function from data release 3. AJ **131**, 2766–2787 (2006).

[3] Wolf, C. *et al.* Discovery of the most ultra-luminous qso using gaia, skymapper, and wise. PASA **35**, e024 (2018).

[4] Pringle, J. E. & Rees, M. J. Accretion disc models for compact x-ray sources. A&A **21**, 1 (1972).

[5] Balbus, S. A. & Hawley, J. F. A powerful local shear instability in weakly magnetized disks. i. linear analysis. ApJ **376**, 214 (1991).

[6] Balbus, S. A. Enhanced angular momentum transport in accretion disks. ARA&A **41**, 555–597 (2003).

[7] Shakura, N. I. & Sunyaev, R. A. Reprint of 1973a&a....24..337s. black holes in binary systems. observational appearance. A&A **500**, 33–51 (1973).

[8] Lawrence, A. Quasar viscosity crisis. *Nature Astronomy* **2**, 102–103 (2018).

[9] Clavel, J. *et al.* Correlated hard x-ray and ultraviolet variability in ngc 5548. ApJ **393**, 113 (1992).

[10] Peterson, B. M. Reverberation mapping of active galactic nuclei. PASP **105**, 247 (1993).

[11] Cackett, E. M., Horne, K. & Winkler, H. Testing thermal reprocessing in active galactic nuclei accretion discs. MNRAS **380**, 669–682 (2007).

[12] Kelly, B. C., Bechtold, J. & Siemiginowska, A. Are the variations in quasar optical flux driven by thermal fluctuations? ApJ **698**, 895–910 (2009).

[13] MacLeod, C. L. *et al.* Modeling the time variability of sdss stripe 82 quasars as a damped random walk. ApJ **721**, 1014–1033 (2010).

[14] Wang, H. & Shi, Y. The deviation of optical variability of radio-quiet quasars from damped random walk. Ap&SS **364**, 27 (2019).

[15] Hughes, P. A., Aller, H. D. & Aller, M. F. The university of michigan radio astronomy data base. i. structure function analysis and the relation between bl lacertae objects and quasi-stellar objects. ApJ **396**, 469 (1992).

[16] Kozłowski, S. Revisiting stochastic variability of agns with structure functions. ApJ **826**, 118 (2016).

[17] Palanque-Delabrouille, N. *et al.* Variability selected high-redshift quasars on sdss stripe 82. A&A **530**, A122 (2011).

[18] Vanden Berk, D. E. *et al.* The ensemble photometric variability of ~25,000 quasars in the sloan digital sky survey. ApJ **601**, 692–714 (2004).

[19] Morganson, E. *et al.* Measuring quasar variability with pan-starrs1 and sdss. ApJ **784**, 92 (2014).

[20] Caplar, N., Lilly, S. J. & Trakhtenbrot, B. Optical variability of agns in the ptf/iptf survey. ApJ **834**, 111 (2017).

[21] Li, Z., McGreer, I. D., Wu, X.-B., Fan, X. & Yang, Q. The ensemble photometric variability of over 10^5 quasars in the dark energy camera legacy survey and the sloan digital sky survey. ApJ **861**, 6 (2018).

[22] Tonry, J. L. *et al.* Atlas: A high-cadence all-sky survey system. PASP **130**, 064505 (2018).

[23] Heckman, T. M. Long-time-scale optical variability in quasars. PASP **88**, 844–848 (1976).

[24] Collaboration, G. *et al.* Gaia early data release 3. summary of the contents and survey properties. A&A **649**, A1 (2021).

[25] Burke, C. J. *et al.* A characteristic optical variability time scale in astrophysical accretion disks. *Science* **373**, 789–792 (2021).

[26] Krawczyk, C. M. *et al.* Mining for dust in type 1 quasars. AJ **149**, 203 (2015).

[27] Weaver, J. R. & Horne, K. Dust and the intrinsic spectral index of quasar variations: hints of finite stress at the innermost stable circular orbit. MNRAS **512**, 899–916 (2022).

[28] Shappee, B. J. *et al.* The man behind the curtain: X-rays drive the uv through nir variability in the 2013 active galactic nucleus outburst in ngc 2617. ApJ **788**, 48 (2014).

[29] Jiang, Y.-F. *et al.* Detection of time lags between quasar continuum emission bands based on pan-starrs light curves. ApJ **836**, 186 (2017).

[30] Fausnaugh, M. M. *et al.* Continuum reverberation mapping of the accretion disks in two seyfert 1 galaxies. ApJ **854**, 107 (2018).

[31] Yu, Z. *et al.* Quasar accretion disk sizes from continuum reverberation mapping in the des standard-star fields. ApJS **246**, 16 (2020).

[32] Yu, W., Richards, G. T., Vogeley, M. S., Moreno, J. & Graham, M. J. Examining agn uv/optical variability beyond the simple damped random walk. *arXiv e-prints* arXiv:2201.08943 (2022).

[33] Frank, J., King, A. & Raine, D. J. *Accretion Power in Astrophysics: Third Edition* (Cambridge University Press, 2002).

[34] Kawaguchi, T., Mineshige, S., Umemura, M. & Turner, E. L. Optical variability in active galactic nuclei: Starbursts or disk instabilities? ApJ **504**, 671–679 (1998).

[35] Kang, W.-y. *et al.* An intrinsic link between long-term uv/optical variations and x-ray loudness in quasars. *Astrophys. J.* **868**, 58 (2018).

[36] Brandt, W. N. *et al.* Active galaxy science in the lsst deep-drilling fields: Footprints, cadence requirements, and total-depth requirements. *arXiv e-prints* arXiv:1811.06542 (2018).

[37] Ivezić, Ž. *et al.* Lsst: From science drivers to reference design and anticipated data products. ApJ **873**, 111 (2019).

[38] Chan, J. H. H., Millon, M., Bonvin, V. & Courbin, F. Twisted quasar light curves: implications for continuum reverberation mapping of accretion disks. A&A **636**, A52 (2020).

[39] Flesch, E. W. The half million quasars (hmq) catalogue. PASA **32**, e010 (2015).

[40] Schlegel, D. J., Finkbeiner, D. P. & Davis, M. Maps of dust infrared emission for use in estimation of reddening and cosmic microwave background radiation foregrounds. ApJ **500**, 525–553 (1998).

[41] Tonry, J. L. *et al.* The atlas all-sky stellar reference catalog. ApJ **867**, 105 (2018).

[42] Riello, M. *et al.* Gaia early data release 3. photometric content and validation. A&A **649**, A3 (2021).

[43] Shen, Y. & Burke, C. J. A sample bias in quasar variability studies. ApJ **918**, L19 (2021).

[44] Becker, R. H., White, R. L. & Helfand, D. J. The first survey: Faint images of the radio sky at twenty centimeters. ApJ **450**, 559 (1995).

[45] Condon, J. J. *et al.* The nrao vla sky survey. AJ **115**, 1693–1716 (1998).

[46] Mauch, T. *et al.* Sumss: a wide-field radio imaging survey of the southern sky - ii. the source catalogue. MNRAS **342**, 1117–1130 (2003).

[47] Blanton, M. R. *et al.* Sloan digital sky survey iv: Mapping the milky way, nearby galaxies, and the distant universe. AJ **154**, 28 (2017).

[48] Yao, S. *et al.* The large sky area multi-object fiber spectroscopic telescope (lamost) quasar survey: The fourth and fifth data releases. ApJS **240**, 6 (2019).

[49] Casagrande, L. & VandenBerg, D. A. On the use of gaia magnitudes and new tables of bolometric corrections. MNRAS **479**, L102–L107 (2018).

[50] Richards, G. T. *et al.* Spectral energy distributions and multiwavelength selection of type 1 quasars. ApJS **166**, 470–497 (2006).

[51] Morgan, C. W., Kochanek, C. S., Morgan, N. D. & Falco, E. E. The quasar accretion disk size-black hole mass relation. ApJ **712**, 1129–1136 (2010).

[52] di Clemente, A., Giallongo, E., Natali, G., Trevese, D. & Vagnetti, F. The variability of quasars. ii. frequency dependence. ApJ **463**, 466 (1996).

Acknowledgements

We thank Mark Krumholz for comments on the manuscript and to Stefan Wagner for helpful discussions. This research was supported by the Australian Research Council (ARC) through Discovery Project DP190100252. It has been funded in part by the Stromlo Distinguished Visitor Program at RSAA. JJT acknowledges support by Institute of Astronomy and Astrophysics, Academia Sinica (ASIAA). This work uses data from the University of Hawaii's ATLAS project, funded through NASA grants NN12AR55G, 80NSSC18K0284, and 80NSSC18K1575, with contributions from the Queen's University Belfast, STScI, the South African Astronomical Observatory, and the Millennium Institute of Astrophysics, Chile. This research has made use of data obtained from LAMOST quasar survey. LAMOST is a National Major Scientific Project built by the Chinese Academy of Sciences. Funding for the project has been provided by the National Development and Reform Commission. LAMOST is operated and managed by the National Astronomical Observatories, Chinese Academy of Sciences.

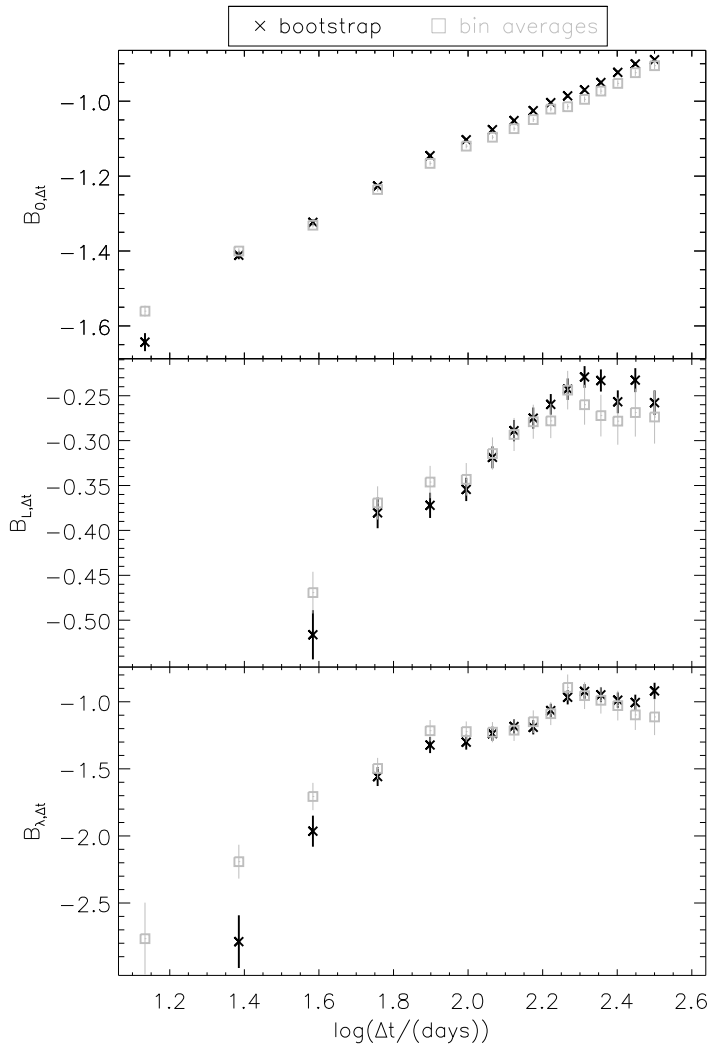

Figure 1: Coefficients of structure function per time interval. $B_{0,\Delta t}$, $B_{L,\Delta t}$ and $B_{\lambda,\Delta t}$ are the fitted results of Equation 10 for each Δt bin. The bootstrap and bin averages results are shown in black and gray, respectively.

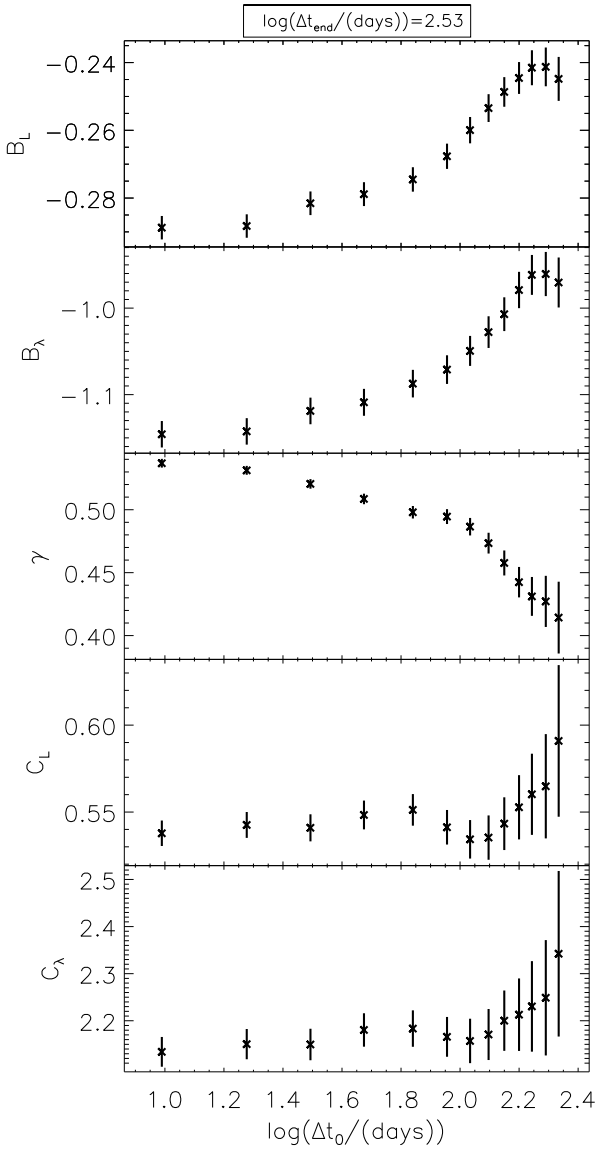

Figure 2: Mean coefficient estimates as a function of Δt window chosen for averaging. Δt_0 is the short end of the fitting window, while the long end of the window is fixed at 337 days. When short timescales are included, the estimates drift, because non-constant behaviour is included into the fit. Shown is the bootstrap case. Restricting the window to the longest timescales, shrinks the data set and makes the fits noisier.

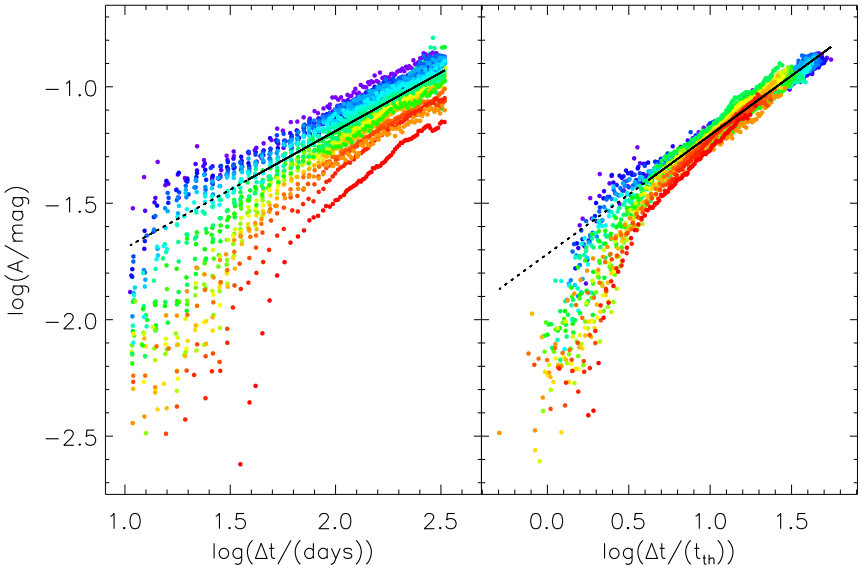

Figure 3: Variability amplitudes $\log A$ vs. $\log \Delta t$ (left) and vs. $\log(\Delta t/t_{\rm th})$ (right). The colour encodes the thermal timescale of the measurement from blue for the shortest to red for the longest $t_{\rm th}$. The best-fit lines to the data at $\log A > -1.4$ have slopes of $\gamma = 0.503$ (left) and $\gamma_{\rm th} = 0.510$ (right), consistent with an undamped random walk. Solid lines show the fit range while the dotted lines are extrapolated. At short Δt, the variability appears suppressed and this effect reaches to longer Δt in larger (here: redder) disks.

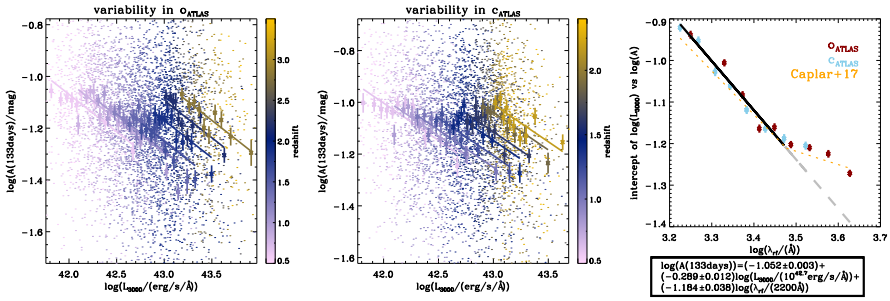

Figure 4: One example time separation bin, $\Delta t_{\rm rest} = [125; 141]$ days. Individual QSOs are points, large symbols are bootstrap mean variability amplitudes in bins of luminosity L_{3000} and redshift z, lines are fits to bootstrap mean values (left: orange passband; centre: cyan passband). Right: intercepts of the fits at fixed L_{3000} for different rest-frame wavelengths, where either passband is seen to sample the same underlying behaviour. Solid lines are fit ranges, dashed lines are extrapolations shown for clarity. Note an upwards deviation at $\lambda > 300$ nm, which is consistent with the dotted line from one past work[20] and also seen in other works[18,32].

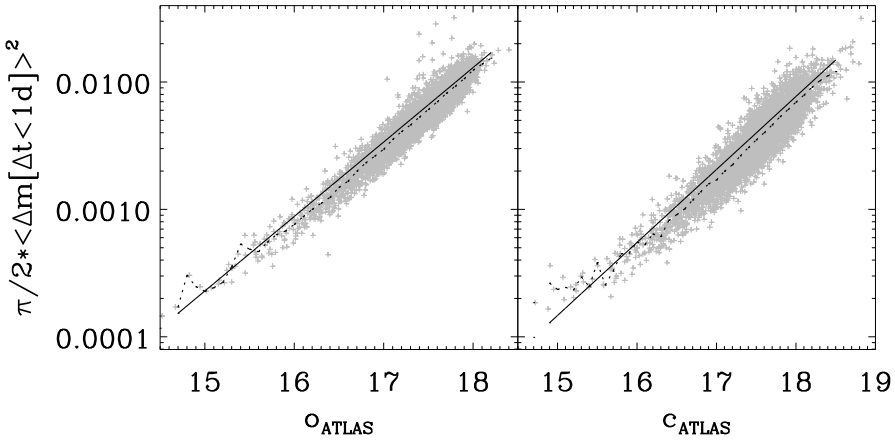

Figure 5: The variability amplitude, $\frac{\pi}{2} < \Delta m >^2$, at $\Delta t < 1$ day as a function of observed magnitude. Gray symbols are individual QSOs. Dotted lines show the 3σ-clipped mean within fine magnitude bins. Solid lines show the fit of Equation 9.